Single-Molecule Magnets: A New Class of Tetranuclear Manganese Magnets

Jae Yoo,[1a] Euan K. Brechin,[1b] Akira Yamaguchi,[1c] Motohiro Nakano,[1a] John C. Huffman,[1b] A. L. Maniero,[1d] Louis-Claude Brunel,[1d] Kunio Awaga,[1e] Hidehiko Ishimoto,*[,1c] George Christou,*[,1b] and David N. Hendrickson*[,1a]

Department of Chemistry and Biochemistry−3058, University of California at San Diego, La Jolla, California 92093, Department of Chemistry and Molecular Structure Center, Indiana University, Bloomington, Indiana 47405, Institute for Solid State Physics, The University of Tokyo, 7-22-1 Roppongi, Minatoku, Tokyo 106-8666, Japan, Center for Interdisciplinary Magnetic Resonance, National High Magnetic Field Laboratory, Tallahassee, Florida 32310, and Department of Basic Science, The University of Tokyo, Komaba, Meguro, Tokyo 153-8902, Japan

Received March 3, 2000

The preparation, X-ray structure, and detailed physical characterization are presented for a new type of single-molecule magnet $[Mn_4(O_2CMe)_2(pdmH)_6](ClO_4)_2$ (**1**). Complex **1**·2MeCN·Et_2O crystallizes in the triclinic space group $P\bar{1}$, with cell dimensions at 130 K of $a = 11.914(3)$ Å, $b = 15.347(4)$ Å, $c = 9.660(3)$ Å, $\alpha = 104.58(1)°$, $\beta = 93.42(1)°$, $\gamma = 106.06(1)°$, and $Z = 1$. The cation lies on an inversion center and consists of a planar Mn_4 rhombus that is mixed-valent, $Mn^{III}_2Mn^{II}_2$. The $pdmH^-$ ligands ($pdmH_2$ is pyridine-2,6-dimethanol) function as either bidentate or tridentate ligands. The bridging between Mn atoms is established by either a deprotonated oxygen atom of a $pdmH^-$ ligand or an acetate ligand. The solvated complex readily loses all acetonitrile and ether solvate molecules to give complex **1**, which with time becomes hydrated to give **1**·2.5H_2O. Direct current and alternating current magnetic susceptibility data are given for **1** and **1**·2.5H_2O and indicate that the desolvated complex has a $S = 8$ ground state, whereas the hydrated **1**·2.5H_2O has a $S = 9$ ground state. Ferromagnetic interactions between $Mn^{III}-Mn^{II}$ and $Mn^{III}-Mn^{III}$ pairs result in parallel spin alignments of the $S = {}^5/_2$ Mn^{II} and $S = 2$ Mn^{III} ions. High-frequency EPR spectra were run for complex **1**·2.5H_2O at frequencies of 218, 328, and 436 GHz in the 4.5−30 K range. A magnetic-field-oriented polycrystallite sample was employed. Fine structure is clearly seen in this parallel-field EPR spectrum. The transition fields were least-squares-fit to give $g = 1.99$, $D = -0.451$ K, and $B_4° = 2.94 \times 10^{-5}$ K for the $S = 9$ ground state of **1**·2.5H_2O. A molecule with a large-spin ground state with $D < 0$ can function as a single-molecule magnet, as detected by techniques such as ac magnetic susceptibility. Out-of-phase ac signals (χ''_M) were seen for complexes **1** and **1**·2.5H_2O to show that these complexes are single-molecule magnets. A sample of **1** was studied by ac susceptibility in the 0.4−6.4 K range with the ac field oscillating at frequencies in the 1.1−1000 Hz range. A single peak in χ''_M vs temperature plots was seen for each frequency; the temperature of the χ''_M peak varies from 2.03 K at 995 Hz to 1.16 K at 1.1 Hz. Magnetization relaxation rates were evaluated in this way. An Arrhenius plot gave an activation energy of 17.3 K, which, as expected, is less than the 22.4 K value calculated for the thermodynamic barrier for magnetization direction reversal for an $S = 8$ complex with $D = -0.35$ K. The **1**·2.5H_2O complex with an $S = 9$ ground state has its χ''_M peaks at higher temperatures.

Introduction

The ultimate in small-size magnetic memory devices is a single-molecule magnet (SMM).[2,3] A SMM has an appreciable potential energy barrier for reversal of the direction of magnetization. In other words, if the magnetic moments of individual molecules in a crystal of a SMM are aligned parallel to an external field, the temperature lowered, and the field then removed, the SMM's would remain magnetized with parallel spins at low temperatures. There are two basic requirements in order for a molecule to function as a SMM. The ground state of the molecule should have a large spin *S*, and there needs to be considerable *negative* anisotropy present. Zero-field splitting in the ground state of a SMM, which arises from single-ion zero-field splitting at the individual metal ions in the molecule, is the origin of the *negative* anisotropy.

The first molecule shown[4−50] to be a SMM was $[Mn_{12}O_{12}(O_2CMe)_{16}(H_2O)_4]$·4$H_2O$·2$HO_2CMe$ (**2**), which exhibits slow magnetization relaxation due to a $S = 10$ ground-state split by axial zero-field splitting ($D\hat{S}_z^2$, where $D = -0.5$ cm^{-1}). In 1996, it was reported[18−21] that complex **2** exhibits quantum mechanical tunneling of the magnetization. Steps were observed at regular

(1) (a) University of California, San Diego. (b) Indiana University. (c) ISSP, The University of Tokyo. (d) National High Magnetic Field laboratory. (e) Department of Basic Science, The Univeristy of Tokyo.
(2) Dahlberg, E. D.; Zhu, J.-G. *Phys. Today* **1995**, 34.
(3) Gunther, L. *Physics World* **1990**, December 28.
(4) Lis, T. *Acta Crystallogr*. **1980**, *B36*, 2042.
(5) Boyd, P. D. W.; Li, Q.; Vincent, J. B.; Folting, K.; Chang, H.-R.; Streib, W. E.; Huffman, J. C.; Christou, G.; Hendrickson, D. N. *J. Am. Chem. Soc.* **1988**, *110*, 8537.
(6) Caneschi, A.; Gatteschi, D.; Sessoli, R.; Barra, A. L.; Brunel, L. C.; Guillot, M. *J. Am. Chem. Soc.* **1991**, *113*, 5873.
(7) Sessoli, R.; Gatteschi, D.; Caneschi, A.; Novak, M. A. *Nature* **1993**, *365*, 141.
(8) Gatteschi, D.; Caneschi, A.; Pardi, L.; Sessoli, R. *Science* **1994**, *265*, 1054.
(9) Villain, J.; Hartman-Boutron, F.; Sessoli, R.; Rettori, A. *Europhys. Lett.* **1994**, *27*, 159.

10.1021/ic000237w CCC: $19.00
Published on Web 07/11/2000

intervals of magnetic field in the magnetization hysteresis loop for oriented crystals of complex **2**. This attracted considerable interest[4−50] in the Mn_{12} complex **2**.

An important current research goal is to prepare new classes of SMM's. In addition to complex **2**, several structurally related dodecanuclear manganese SMM's have been characterized with the composition $[Mn_{12}O_{12}(O_2CR)_{16}(H_2O)_4]$.[51−59] These Mn_{12} complexes can be reduced by one electron to give $S = {}^{19}/_{2}$ complexes that function as SMM's with the composition [cation]-$[Mn_{12}O_{12}(O_2CR)_{16}(H_2O)_4]$.[60,61] Quantum tunneling of the magnetization has also been observed for these $S = {}^{19}/_{2}$ SMM's. A third class of SMM's consists of distorted cubane complexes with the $[Mn^{IV}Mn^{III}_3O_3X]^{6+}$ core.[62,63] Tetranuclear vanadium butterfly complexes, $[V_4O_2(O_2CR)_7(L)_2]^n$, where L is either bipyridine or picolinate, comprise the fourth class of SMM's.[64] Finally, two different iron complexes, $[Fe_8O_2(OH)_{12}(tacn)_6]^{8+}$ where tacn is a tetraaza macrocyclic ligand,[65] and $[Fe_4(OCH_3)_6(dpm)_6]$ where dpmH is dipivaloylmethane,[66] have been found to function as single-molecule magnets.

In this paper, we report the preparation and characterization of a new class of SMM, namely, the cationic complex in $[Mn_4(O_2CMe)_2(pdmH)_6](ClO_4)_2$ (**1**), which is shown to function as a SMM. It is of particular interest to compare the properties of complex **1** to those reported[63] for $[Mn_4O_3Cl(O_2CCH_3)_3(dbm)_3]$ (**3**), where dbm^- is the monoanion of dibenzoylmethane. Complex **3** has a $S = {}^{9}/_{2}$ ground state with $D = -0.53\ cm^{-1}$ and was shown to have an activation energy of 11.8 K for reversal of the direction of magnetization. In this report, complex **1** is shown to have a ground state of either $S = 8$ or $S = 9$, depending upon whether the complex is free of solvate molecules or hydrated.

Experimental Section

Synthesis. All manipulations were carried out under aerobic conditions using solvents as received. Pyridine-2,6-dimethanol ($pdmH_2$; 2,6-

(10) Barra, A. L.; Caneschi, A.; Gatteschi, D.; Sessoli, R. *J. Am. Chem. Soc.* **1995**, *117*, 8855.
(11) Novak, M. A.; Sessoli, R.; Caneschi, A.; Gatteschi, D. *J. Magn. Magn. Mater.* **1995**, *146*, 211.
(12) Barbara, B.; Wernsdorfer, W.; Sampaio, L. C.; Park, J. G.; Paulsen, C.; Novak, M. A.; Ferre, R.; Mailly, D.; Sessoli, R.; Caneschi, A.; Hasselbach, K.; Benoit, A.; Thomas, L. *J. Magn. Magn. Mater.* **1995**, *140*−*144*, 1825.
(13) Novak, M. A.; Sessoli, R. In *Quantum Tunneling of Magnetization*—*QTM '94*. Gunter, L., Barbara, B., Eds.; Kluwer Academic Publishers: Dordrecht, 1995; pp 171−188.
(14) Paulsen, C.; Park, J. G. In *Quantum Tunneling of Magnetization*—*QTM '94*. Gunther, L., Barbara, B., Eds.; Kluwer Academic Publishers: Dordrecht, 1995; pp 189−207.
(15) Paulsen, C.; Park, J. G.; Barbara, B.; Sessoli, R.; Caneschi, A. *J. Magn. Magn. Mater.* **1995**, *140*−*144*, 1891.
(16) Friedman, J. R. Ph.D. Thesis, The City College of New York, New York, NY, 1996.
(17) Politi, R.; Rettori, A.; Hartmann-Boutron, F.; Villain, J. *Phys. Rev. Lett.* **1995**, *75*, 537.
(18) Friedman, J. R.; Sarachik, M. P.; Tejada, J.; Maciejewski, J.; Ziolo, R. *J. Appl. Phys.* **1996**, *79*, 6031.
(19) Friedman, J. R.; Sarachik, M. P.; Tejada, J.; Ziolo, R. *Phys. Rev. Lett.* **1996**, *76*, 3830.
(20) Thomas, L.; Lionti, F.; Ballou, R.; Gatteschi, D.; Sessoli, R.; Barbara, B. *Nature* **1996**, *383*, 145.
(21) Tejada, J.; Ziolo, R. F.; Zhang, X. X. *Chem. Mater.* **1996**, *8*, 1784.
(22) Hernandez, J. M.; Zhang, X. X.; Luis, F.; Bartolome, J.; Tejada, J.; Ziolo, R. *Europhys. Lett.* **1996**, *35*, 301.
(23) Chudnovsky, E. M. *Science* **1996**, *274*, 938.
(24) Reynolds, P. A.; Gilber, E. P.; Figgis, B. N. *Inorg. Chem.* **1996**, *35*, 545.
(25) Gatteschi, D. *Curr. Opin. Solid State Mater. Sci.* **1996**, *1*, 192.
(26) Burin, A. L.; Prokof'ev, N. V.; Stamp, P. C. E. *Phys. Rev. Lett.* **1996**, *76*, 3040.
(27) Politi, R.; Rettori, A.; Hartmann-Boutron, F.; Villain, J. *Phys. Rev. Lett.* **1996**, *76*, 3041.
(28) Schwarzschild, B. *Phys. Today* **1997**, January 17.
(29) Lionti, F.; Thomas, L.; Ballou, R.; Barbara, B.; Sulpice, A.; Sessoli, R.; Gatteschi, D. *J. Appl. Phys.* **1997**, *81*, 4608.
(30) Friedman, J. R.; Sarachik, M. P.; Hernandez, J. M.; Zhang, X. X.; Tejada, J.; Molins, E.; Ziolo, R. *J. Appl. Phys.* **1997**, *81*, 3978.
(31) Barra, A. L.; Gatteschi, D.; Sessoli, R. *Phys. Rev. B* **1997**, *56*, 8192.
(32) Luis, F.; Bartolome, J.; Fernandez, J. F. *Phys. Rev. B* **1997**, *55*, 11448.
(33) Hernandez, J. M.; Zhang, X. X.; Luis, F.; Tejada, J.; Friedman, J. R.; Sarachik, M. P.; Ziolo, R. *Phys. Rev. B* **1997**, *55*, 5858.
(34) Cheesman, M. R.; Oganesyan, V. S.; Sessoli, R.; Gatteschi, D.; Thompson, A. *Chem. Commun.* **1997**, 1677.
(35) Caneschi, A.; Gatteschi, D.; Sessoli, R. *J. Chem. Soc., Dalton Trans.* **1997**, 3963.
(36) Zhang, X. X.; Tejada, J.; Hernandez, J. M.; Ziolo, R. F. *Nanostruct. Mater.* **1997**, *9*, 301.
(37) Chudnovsky, E. M.; Garanin, D. A. *Phys. Rev. Lett.* **1997**, *79*. 4469.
(38) Garanin, D. A.; Chudnovsky, E. M. *Phys. Rev. B* **1997**, *56*, 11102.
(39) Wei, Y.-G.; Zhang, S.-W.; Shao, M.-C.; Tang, Y.-Q. *Polyhedron* **1997**, *16*, 1471.
(40) Forminya, F.; Villain, J.; Gandit, P.; Chaussy, J.; Caneschi, A. *Phys. Rev. Lett.* **1997**, 79, 1126.
(41) Fort, A.; Rettori, A.; Villain, J.; Gatteschi, D.; Sessoli, R. *Phys. Rev. Lett.* **1998**, *80*, 612.
(42) Lascialfari, A.; Gatteschi, D.; Borsa, F.; Shastri, A.; Jang, Z. H.; Carretta, P. *Phys. Rev. B* **1998**, *57*, 514.
(43) Hill, S.; Perenboon, J. A. A. J.; Dalal, N. S.; Hathaway, T.; Stalcup, T.; Brooks, J. S. *Phys. Rev. Lett.* **1998**, *80*, 2453.
(44) Luis, F.; Bartolome, J.; Fernandez, J. F. *Phys. Rev. B* **1998**, *57*, 505.
(45) Lascialfari, A.; Jang, Z. H.; Borsa, F.; Carretta, P.; Gatteschi, D. *Phys. Rev. Lett.* **1998**, *81*, 3773.
(46) Pederson, M. R.; Khanna, S. N. *Phys. Rev B* **1999**, *59*, 693.
(47) Zhong, Y.; Sarachik, M. P.; Friedman, J. R.; Robinson, R. A.; Kelley, T. M.; Nakotte, H.; Christianson, A. C.; Trouw, F.; Aubin, S. M. J.; Hendrickson, D. N. *J. App. Phys.* **1999**, *85*, 5636.
(48) Leuenberger, M. N.; Loss, D. *Europhys. Lett.* **1999**, *46*, 692.
(49) Mirebeau, I.; Hennion, M.; Casalta, H.; Andres, H.; Gudel, H. U.; Irodova, A. V.; Caneschi, A. *Phys. Rev. Lett.*, in press.
(50) Wernsdorfer, W.; Sessoli, R.; Gatteschi, D. *Europhys. Lett.*, in press.
(51) Eppley, H. J.; Wang, S.; Tsai, H.-L.; Aubin, S. M. J.; Folting, K.; Streib, W. E.; Hendrickson, D. N.; Christou, G. *Mol. Cryst. Liq. Cryst.* **1995**, *274*, 159.
(52) Tsai, H.-L.; Eppley, H. J.; de Vries, N.; Folting, K.; Christou, G.; Hendrickson, D. N. *Mol. Cryst. Liq. Cryst.* **1995**, *274*, 167.
(53) Aubin, S. M. J.; Spagna, S.; Eppley, H. J.; Sager, R. E.; Folting, K.; Christou, G.; Hendrickson, D. N. *Mol. Cryst. Liq. Cryst.* **1997**, *305*, 181.
(54) Eppley, H. J.; Aubin, S. M. J.; Wemple, M. W.; Adams, D. M.; Tsai, H.-L.; Grillo, V. A.; Castro, S. L.; Sun, Z.; Folting, K.; Huffman, J. C.; Hendrickson, D. N.; Christou, G. *Mol. Cryst. Liq. Cryst.* **1997**, *305*, 167.
(55) Schake, A. R.; Tsai, H.-L.; de Vries, N.; Webb, R. J.; Folting, K.; Hendrickson, D. N.; Christou, G. *Chem. Commun.* **1992**, 181.
(56) Sessoli, R.; Tsai, H.-L.; Schake, A. R.; Wang, S.; Vincent, J. B.; Folting, K.; Gatteschi, D.; Christou, G.; Hendrickson, D. N. *J. Am. Chem. Soc.* **1993**, *115*, 1804.
(57) Ruiz, D.; Sun, Z.; Albela, B.; Folting, K.; Ribas, J.; Christou, G.; Hendrickson, D. N. *Angew. Chem., Int. Ed.* **1998**, *37*, 300.
(58) Aubin, S. M. J.; Sun, Z.; Guzei, I. A.; Rheingold, A. L.; Christou, G.; Hendrickson, D. N. *Chem. Commun.* **1997**, 2239.
(59) Sun, Z.; Ruiz, D.; Rumberger, E.; Incarvito, C. D.; Folting, K.; Rheingold, A. L.; Christou, G.; Hendrickson, D. N. *Inorg. Chem.* **1998**, *37*, 4758.
(60) Eppley, H. J.; Tsai, H.-L.; de Vries, N.; Folting, K.; Christou, G.; Hendrickson, D. N. *J. Am. Chem. Soc.* **1995**, *117*, 301.
(61) Aubin, S. M. J.; Spagna, S.; Eppley, H. J.; Sager, R. E.; Christou, G.; Hendrickson, D. N. *Chem. Commun.* **1998**, 803.
(62) Aubin, S. M. J.; Wemple, M. W.; Adams, D. M.; Tsai, H.-L.; Christou, G.; Hendrickson, D. N. *J. Am. Chem. Soc.* **1996**, *118*, 7746.
(63) (a) Aubin, S. M. J.; Dilley, N. R.; Wemple, M. W.; Maple, M. B.; Christou, G.; Hendrickson, D. N. *J. Am. Chem. Soc.* **1998**, *120*, 839. (b) Aubin, S. M. J.; Dilley, N. R.; Pardi, L.; Krzystek, J.; Wemple, M. W.; Brunel, L.-C.; Maple, M. B.; Christou, G.; Hendrickson, D. N. *J. Am. Chem. Soc.* **1998**, *120*, 4991.
(64) (a) Sun, Z.; Castro, S. L.; Bollinger, J. C.; Hendrickson, D. N.; Christou, G. *Chem. Commun.* **1995**, 2517. (b) Castro, S. L.; Sun, Z.; Grant, C. M.; Bollinger, J. C.; Hendrickson, D. N.; Christou, G. *J. Am. Chem. Soc.* **1998**, *120*, 2365.
(65) Barra, A.-L.; Debrunner, P.; Gatteschi, D.; Schulz, Ch. E.; Sessoli, R. *Europhys. Lett.* **1996**, *35*, 133.
(66) Barra, A. L.; Caneschi, A.; Cornia, A.; Fabrizi de Biani, F.; Gatteschi, D.; Sangregorio, C.; Sessoli, R.; Sorace, L. *J. Am. Chem. Soc.* **1999**, *121*, 5302.

bis(hydroxymethyl)pyridine, Aldrich) was used as received. $[Mn_3O(O_2CMe)_6(py)_3](ClO_4)$ (**4**) was prepared as described elsewhere.[67]

$[Mn_4(OAc)_2(pdmH)_6](ClO_4)_2$ (1). a. Method 1. Complex **4** (0.500 g, 0.574 mmol) and $pdmH_2$ (0.240 g, 1.72 mmol) were dissolved in CH_2Cl_2 (30 mL), and the resultant red-brown solution was stirred overnight at room temperature. During this time, a fine brown precipitate slowly formed, and this was collected by filtration, washed with a little CH_2Cl_2, redissolved in MeCN (20 mL), and the solution filtered. The filtrate was layered with Et_2O to slowly give well-formed brown crystals. After 3 days they were collected by filtration, washed with Et_2O, and dried in vacuo. The yield was ~50%. Dried solid was analyzed to be solvent-free. Anal. Calcd (Found) for $C_{46}H_{54}Cl_2Mn_4N_6O_{24}$: C, 40.42 (40.50); H, 3.95 (4.10); N, 6.15 (6.04). Selected IR data (cm^{-1}): 1605 (s), 1582 (s), 1464 (m), 1447 (m), 1381 (m), 1331 (m), 787 (m), 691 (m), 666 (m), 627 (m). The crystallographic sample was maintained in contact with the mother liquor to prevent solvent loss, and it was identified crystallographically as **1**·2MeCN·Et_2O. In contact with air, complex **1** becomes hydrated to give complex **1**·2.5H_2O. Anal. Calcd (Found) for $C_{46}H_{54}Cl_2Mn_4N_6O_{24}$·2.5$H_2O$: C, 39.12 (39.11); H, 4.04 (3.88); N, 5.95 (6.13).

b. Method 2. Complex **4** (0.500 g, 0.574 mmol) and $pdmH_2$ (0.240 g, 1.72 mmol) were dissolved in MeCN (30 mL) and the solution stirred overnight at room temperature. No precipitate was obtained. The solution was filtered and the filtrate layered with Et_2O to give brown crystals, which were isolated after 7 days, washed with Et_2O, and dried in vacuo. The yield was 15%, and the solid was spectroscopically (IR) identical with that from Method 1.

X-ray Crystallography. X-ray crystallographic data were collected on a Picker four-circle diffractometer at low temperature. A suitable crystal was affixed to the end of a glass fiber using silicone grease and rapidly transferred to the goniostat where it was cooled for characterization and data collection. Details of the diffractometry, low-temperature facilities, and computational procedures employed by the Molecular Structure Center are available elsewhere.[68] The structure was solved by direct methods (SHELXTL) and Fourier methods and refined on *F* by full-matrix least-squares cycles.

A systematic search of a limited hemisphere of reciprocal space revealed that the crystal possessed no symmetry or systematic absences, indicating a triclinic space group. Subsequent solution and refinement confirmed the centrosymmetric choice, $P\bar{1}$. After data collection ($+h$, $\pm k$, $\pm l$; $6° < 2\theta < 50°$) and processing, and averaging of reflections measured more than once ($R_{av} = 0.198$), the structure was solved without serious problems. The Mn_4 cation lies at a center of inversion, and a disordered solvate molecule is present in addition to the ordered ClO_4^- anions and MeCN solvate molecules. Oxygen O(23), which is not bound to a Mn, was disordered about two (main) positions and the occupancies refined to 74% and 15% (the main position is shown in Figure 1). The disordered solvate molecule was modeled as seven closely spaced C atoms and was assumed to be a badly disordered Et_2O molecule. In the final refinement cycles, non-hydrogen atoms were refined anisotropically except for the minor disorder position of O(23) and the solvate molecules. Hydrogen atoms were included for the cation in fixed, idealized positions with thermal parameters of 1.0 plus the isotropic thermal parameter of the parent atom. A final difference Fourier map was featureless, the largest peaks of intensity 1.05 e/Å^3 lying in the vicinity of the ClO_4^- anions and disordered solvent molecule. Final *R* and R_w values are listed in Table 1.

Physical Methods. IR measurements were made on samples pressed into KBr pellets using a Nicolet model 510P spectrophotometer. Direct current magnetic susceptibility experiments were performed on powdered microcrystalline samples (restrained in eicosane to prevent torquing at high fields) on a Quantum Design MPMS superconducting quantum interference device (SQUID) magnetometer equipped with a 5.5 T (55 kG) magnet and capable of operating in the 1.7−400 K range. Diamagnetic contributions to the susceptibility were corrected using Pascal's constants.

(67) Vincent, J. B.; Chang, H.-R.; Folting, K.; Huffman, J. C.; Christou, G.; Hendrickson, D. N. *J. Am. Chem. Soc*. **1987**, *109*, 5703.
(68) Chisholm, M. H.; Folting, K.; Huffman, J. C.; Kirkpatrick, C. C. *Inorg. Chem*. **1984**, *23*, 1021.

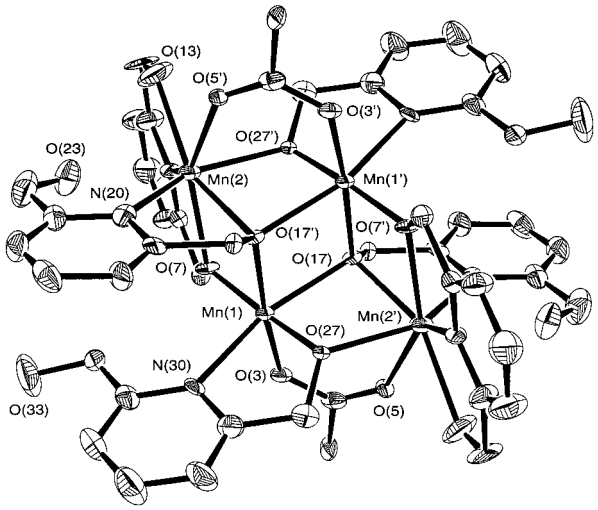

Figure 1. ORTEP plot of the $[Mn_4(O_2CCH_3)_2(pdmH)_6]^{2+}$ cation in complex **1**·2MeCN·2Et_2O.

Table 1. Crystallographic Data for $[Mn_4(O_2CMe)_2(pdmH)_6](ClO_4)_2$·2MeCN·$Et_2O$.

formula	$C_{50}H_{60}Cl_2Mn_4N_8O_{24}$[a]	fw, g mol^{-1}	1447.75
a, Å	11.914(3)	space group	$P\bar{1}$
b, Å	15.347(4)	temp, °C	−168
c, Å	9.660(3)	λ, Å	0.710 69[b]
α, deg	104.58(1)	ρ_{cald}, g/cm^3	1.628
β, deg	93.42(1)	μ(Mo Kα), cm^{-1}	9.315
γ, deg	106.06(1)	R[c]	0.0871
V, Å^3	1626 Å^3	R_w[d]	0.0679
Z	1		

[a] Excluding Et_2O molecule. [b] Graphite monochromator. [c] $R_w = [\sum w(|F_o| - |F_c|)^2/\sum w|F_o|^2]^{1/2}$ where $w = 1/s^2(|F_o|)$.

The ac magnetic susceptibility experiments above 1.7 K were carried out on a Quantum Design MPMS2 SQUID magnetometer. The ac field strength can be varied from 0.001 to 5 G at frequencies ranging from 0.0005 to 1512 Hz. The temperature range available is 1.7−400 K. Low-temperature ac magnetic susceptibility experiments down to the millikelvin temperature range were performed at the Institute of Solid State Physics, University of Tokyo. Measurements were made on a SHE-RLM bridge where a SQUID served as a null detector. Measurements were made on a powdered microcrystalline sample stuck on a quartz glass with a small amount of Apiezon N grease to reduce the background signal. It was immersed in nonmagnetic liquid ^{4}He, which was cooled by way of a sintered powder heat exchanger with a ^{3}He−^{4}He dilution refrigerator. The temperature was determined with germanium and carbon resistor thermometers. Thermal contact between the sample and the coolant was found to be good enough because the susceptibility of the sample quickly followed the temperature change of the refrigerator. Data were collected in the 1.1−995 Hz frequency range between 0.4 and 3.5 K.

High-frequency EPR spectra were recorded at the National High Magnetic Field Laboratory, Tallahassee, Florida. The spectrometer is equipped with a 14.5 T superconducting magnet and can achieve temperatures ranging from 4 to 300 K. In this work, a Gunn diode operating at a fundamental frequency of 110 ± 3 GHz was used. The operating frequency range is 110−550 GHz. Frequencies between 220 and 550 GHz were obtained by using a solid-state harmonic generator that multiplies the fundamental frequency (i.e., 110 GHz) and high-pass filters to filter out the lower frequency harmonics and to allow the higher frequency harmonics to pass through. A modulation frequency of 8.5 kHz was used for phase-sensitive detection. The magnetic field was swept at a rate of 0.2 T/min over a 0−14.5 T range.

Results and Discussion

Synthesis. The pyridine-2,6-dimethanol group has been little explored as a chelating ligand in metal chemistry. It has been

observed in its doubly deprotonated (pdm^{2-}) form as a tridentate chelate in $[MoO_2(pdm)]_n$, a linear polymer,[69] but it more commonly occurs in its singly deprotonated ($pdmH^-$) form as a bidentate chelate with the protonated oxygen not bound. This ligation mode is found in $[TcOCl(pdmH)_2]$[70] and $[ReOCl_2(PPh_3)(pdmH)]$.[71] In $[PtCl_2(pdmH_2)_2]$, it acts as a monodentate ligand through the pyridine N atom and both protonated O atoms are unligated.[72] It thus appeared timely to investigate the reactions of $pdmH_2$ with Mn carboxylate species such as complex **4**, especially since related reactions with 2-(hydroxymethyl)pyridine are also under exploration by us.[73,74]

Treatment of Mn_3 complex **4** with 3 equiv of $pdmH_2$ in CH_2Cl_2 gave a slight color change to an orange-brown and the slow formation of a brown precipitate. This was recrystallized from $MeCN/Et_2O$ and identified as $[Mn_4(O_2CMe)_2(pdmH)_6](ClO_4)_2$ (**1**). The same reaction in MeCN also gave complex **1** but in only ~15% yield compared with ~50% in CH_2Cl_2. The product contains a pdmH/Mn ratio of 1.5:1, whereas the reaction solution had a ratio of 1:1; however, attempts to increase the yield by increasing the $pdmH_2$/Mn reaction ratio gave a mixture of products and were not further pursued. The 50% yield of product actually corresponds to a 67% yield based on available $pdmH^-$, as summarized in eqn(1).

$$4[Mn_3O]^{7+} + 12pdmH_2 \xrightarrow[+4e^-]{} 2[Mn_4(pdmH)_6]^{4+} + 4Mn^{3+} + 4H_2O + 4H^+ \quad (1)$$

The formulation of **1** requires a $2Mn^{II}$, $2Mn^{III}$ oxidation state description; this was determined by consideration of the structural parameters (see below) and bond valence sum (BVS) calculations.[75] The source of the reducing equivalents is unclear; some Mn^{III} is disproportionating to Mn^{II} and Mn^{IV} or solvent and/or ligand oxidation by strongly oxidizing Mn^{III} is occurring. Similar uncertainties in the source of reducing equivalents are often encountered in Mn^{III} chemistry.[76]

Description of Structure. A labeled ORTEP plot and stereoview of the cation of $[Mn_4(O_2CMe)_2(pdmH)_6](ClO_4)_2$ (**1**) are provided in Figure 1. Selected interatomic distances and angles are listed in Table 2. Complex **1**·2MeCN·Et_2O crystallizes in triclinic space group $P\bar{1}$, the cation lying on an inversion center and consisting of an exactly planar Mn_4 rhombus. Each Mn_3 triangular unit is μ_3-bridged by an oxygen atom O(17) from a bidentate chelating $pdmH^-$ group whose protonated O(23) is unbound. Two of the remaining $pdmH^-$ groups are also bidentate, with O(27) bridging Mn(1) and Mn(2′) and O(33) not ligated, but the remaining two $pdmH^-$ groups are tridentate with protonated O(13) terminally coordinated and O(7) bridging Mn(1) and Mn(2). Two bridging $MeCO_2^-$ groups complete the ligation and make Mn(1) and Mn(2) six- and seven-coordinate, respectively. Inspection of structural parameters identifies Mn(1) and Mn(2) as Mn^{III} and Mn^{II}, respectively. Mn(1) displays a Jahn−Teller distortion as expected for high-spin d^4 ion in near-octahedral geometry, taking the form of an elongation of the O(17)−Mn(1)−N(30) and symmetry-related O(17′)−Mn(1′)−N(30′) axes. Thus, Mn(1)−O(17) [2.264(4) Å] and Mn(1)−N(30) [2.319(6) Å] are distinctly longer than the other four bond lengths [1.879(5)−1.967(4) Å]. The Mn^{II} assignment for Mn(2) is also evident from the longer Mn−ligand bond lengths (average 2.287 Å) compared with those to Mn(1) (average 2.043 Å), although this is also as expected from the greater coordination number. Therefore, BVS calculations were performed, and the obtained values of 2.94 for Mn(1) and 1.84 for Mn(2) confirm the Mn^{III} and Mn^{II} oxidation states, respectively. The geometry at Mn(2) is distorted pentagonal bipyramidal, with N(20)−Mn(2)−O(27′) being the axis, and there is an intramolecular hydrogen bond between O(213) and O(13) [2.852(9) Å].

Table 2. Selected Interatomic Distances (Å) and Angles (deg) for $[Mn_4(O_2CMe)_2(pdmH)_6](ClO_4)_2$·MeCN·$2Et_2O$

Mn(1)	O(3)	1.957(5)	Mn(2)	O(7)	2.271(4)		
Mn(1)	O(7)	1.879(5)	Mn(2)	O(13)	2.283(5)		
Mn(1)	O(17′)	1.967(4)	Mn(2)	O(17)	2.300(5)		
Mn(1)	O(17)	2.264(4)	Mn(2)	O(27)	2.227(4)		
Mn(1)	O(27)	1.873(5)	Mn(2)	N(10)	2.272(6)		
Mn(1)	N(30)	2.319(6)	Mn(2)	N(20)	2.310(6)		
Mn(2)	O(5)	2.346(5)					
O(3)	Mn(1)	O(7)	93.86(20)	O(17)	Mn(1)	N(30)	99.01(19)
O(3)	Mn(1)	O(17)	170.17(19)	O(17′)	Mn(1)	N(30)	161.01(19)
O(3)	Mn(1)	O(17′)	91.95(17)	O(27)	Mn(1)	N(30)	77.61(20)
O(3)	Mn(1)	O(27)	94.78(20)	O(5)	Mn(2)	O(7)	145.23(17)
O(3)	Mn(1)	N(30)	90.56(19)	O(5)	Mn(2)	O(13)	73.12(20)
O(7)	Mn(1)	O(17)	82.10(19)	O(5)	Mn(2)	O(17)	78.59(16)
O(7)	Mn(1)	O(17′)	97.03(18)	O(5)	Mn(2)	O(27)	78.53(17)
O(7)	Mn(1)	O(27)	171.33(21)	O(5)	Mn(2)	N(10)	138.60(18)
O(7)	Mn(1)	N(30)	101.58(20)	O(5)	Mn(2)	N(20)	80.99(19)
O(17)	Mn(1)	O(17′)	79.73(17)	O(7)	Mn(2)	O(13)	139.24(22)
O(17)	Mn(1)	O(27′)	89.48(19)	O(7)	Mn(2)	O(17)	67.10(16)
O(17)	Mn(1)	O(27)	83.43(18)	O(7)	Mn(2)	O(27)	87.35(16)
O(7)	Mn(2)	N(10)	70.26(19)	O(17)	Mn(2)	N(20)	70.72(18)
O(7)	Mn(2)	N(20)	92.44(19)	O(27)	Mn(2)	N(10)	85.60(19)
O(13)	Mn(2)	O(17)	150.41(19)	O(27)	Mn(2)	N(20)	143.15(21)
O(13)	Mn(2)	O(27)	90.47(19)	N(10)	Mn(2)	N(20)	128.79(21)
O(13)	Mn(2)	N(10)	69.00(22)	Mn(1)	O(7)	Mn(2)	107.30(23)
O(13)	Mn(2)	N(20)	112.36(22)	Mn(1)	O(17)	Mn(1)	100.27(17)
O(17)	Mn(2)	O(27)	75.39(16)	Mn(1)	O(17)	Mn(2)	92.03(16)
O(17)	Mn(2)	N(10)	133.70(18)	Mn(1)	O(17)	Mn(2)	103.24(20)

It is important for the HFEPR studies to note that the cationic complexes in **1**·2MeCN·Et_2O are packed in the crystal such that all molecules are oriented parallel to each other.

Different Forms of Complex 1. During the course of study of this Mn_4 complex it was discovered that there are at least three different forms of complex **1**. There is the form characterized in the X-ray structure as the solvated complex $[Mn_4(O_2CMe)_2(pdmH)_6](ClO_4)_2$·2MeCN·$Et_2O$ (**1**·2MeCN·$2Et_2O$). This form readily loses the solvate molecules to give the nonsolvated complex **1**. Finally, if the nonsolvated complex is in contact with air for several weeks, it becomes hydrated to give a complex with the approximate composition $[Mn_4(O_2CMe)_2(pdmH)_6](ClO_4)_2$·$2.5H_2O$ (**1**·$2.5H_2O$). It is shown that there are differences in the properties of **1** and **1**·$2.5H_2O$.

Loss of the MeCN and Et_2O solvate molecules was detected by use of IR spectra and chemical analysis. Hydration of complex **1** to give **1**·$2.5H_2O$ was established by chemical analysis of the hydrated complex and by thermogravimetric analysis (tga) of **1**·$2.5H_2O$. A weight loss of 3.1% was found in a tga run, and this gave a formulation of **1**·$2.5H_2O$.

Direct Current Magnetic Susceptibility. Variable-temperature magnetic susceptibility measurements were made on

(69) Berg, J. M.; Holm, R. H. *Inorg. Chem.* **1983**, *22*, 1768.
(70) Rochon, F. D.; Melanson, R.; Kong, P.-C. *Inorg. Chim. Acta* **1997**, *254*, 303.
(71) Gerber, T. I. A.; Bruwer, J.; Bandoli, G.; Perils, J.; du Preez, J. G. H. *J. Chem. Soc., Dalton Trans.* **1995**, 2189.
(72) Rochon, F. D.; Beauchamp, A. L.; Bensimon, C. *Can. J. Chem.* **1996**, *74*, 2121.
(73) Bolcar, M. A.; Aubin, S. M. J.; Folting, K.; Hendrickson, D. N.; Christou, G. *J. Chem. Soc., Chem. Commun.* **1997**, 1485.
(74) Brechin, E. K.; Yoo, J.; Bolcar, M. A.; Hendrickson, D. N.; Christou, G. Unpublished results.
(75) (a) Brown, I. D.; Altermatt, D. *Acta Crystallogr., Sect. B* **1985**, *41*, 244. (b) Brown, I. D. *Solid State Chem.* **1989**, *82*, 122. (c) Thorpe, H. H. *Inorg. Chem.* **1992**, *31*, 1585.
(76) Wemple, M. W.; Tsai, H.-L.; Wang, S.; Claude, J. P.; Streib, W. E.; Huffman, J. C.; Hendrickson, D. N.; Christou, G. *Inorg. Chem.* **1996**, *35*, 6450.

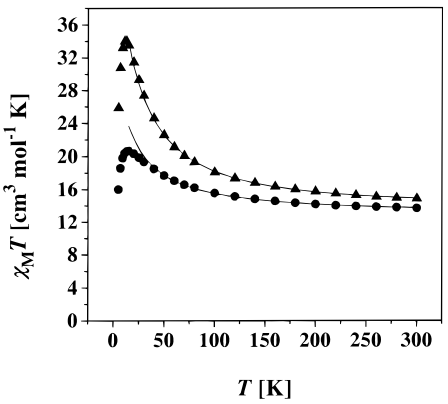

Figure 2. Plot of $\chi_M T$ vs temperature for polycrystalline samples of the nonsolvated complex **1** (●) and the hydrated complex **1**·2.5H_2O (▲). χ_M is the dc magnetic susceptibility measured in a 10 kG field. The solid lines represent the least-squares fit of the data to a Kambe model. See the text for a discussion of the model and the fitting parameters.

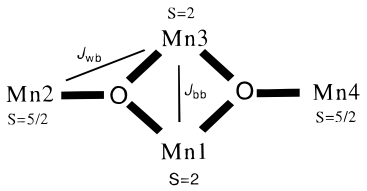

Figure 3. Diagram showing the definition of atom number and magnetic exchange parameters for complex **1**.

powdered polycrystalline samples of the desolvated complex **1**, restrained in eicosane to prevent torquing, in a 10 kG applied magnetic field in the 5.00−300 K range. Figure 2 gives a plot of $\chi_M T$ vs temperature. The value of $\chi_M T$ is 13.68 cm^3 mol^{-1} K at 300 K and is slightly below the spin-only value of 14.75 cm^3 mol^{-1} K expected for a complex consisting of two Mn^{II} and two Mn^{III} noninteracting ions. At lower temperatures, $\chi_M T$ slowly increases to a maximum of 20.65 cm^3 mol^{-1} K at 15.0 K, whereupon it decreases to 16.00 cm^3 mol^{-1} K at 5.00 K. If there are no intermolecular ferromagnetic exchange interactions, this increase in $\chi_M T$ at lower temperatures is a clear indication of a large-spin ground state. Similar dependencies of $\chi_M T$ upon temperature have been observed for Mn_4,[63] Mn_{12},[60] and Mn_7[77] complexes that have been determined to have $S = {}^9/_2$, $S = 10$, and $S = 11$ ground states, respectively. The decrease in $\chi_M T$ observed at low temperatures is likely due to zero-field splitting and/or Zeeman effects.

The $\chi_M T$ vs temperature data for the desolvated complex **1** were fit in order to determine the magnetic exchange interactions. Owing to the low symmetry of **1**, three different types of exchange pathways exist, making it impossible to employ the Kambe vector coupling approach. As an initial approximation, the experimental $\chi_M T$ vs temperature data were least-squares-fit using a model where only two dominant exchange pathways were considered (Figure 3). This approximation equates $J_{12} = J_{23} \equiv J_{wb}$. This enabled us to use the Kambe vector coupling method to derive the following spin Hamiltonian:

$$\hat{H} = -J_{wb}(\hat{S}_T^{\,2} - \hat{S}_A^{\,2} - \hat{S}_B^{\,2}) - J_{bb}(\hat{S}_A^{\,2} - \hat{S}_1^{\,2} - \hat{S}_3^{\,2}) \quad (2)$$

where $\hat{S}_A = \hat{S}_1 + \hat{S}_3$, $\hat{S}_B = \hat{S}_2 + \hat{S}_4$, and $\hat{S}_T = \hat{S}_A + \hat{S}_B$.

The corresponding eigenvalue expression is given in

$$E(S_T) = -J_{wb}[S_T(S_T + 1) - S_A(S_A + 1) - S_B(S_B + 1)] - J_{bb}[S_A(S_A + 1)] \quad (3)$$

With two $S = 2$ and two $S = {}^5/_2$ interacting ions there are a total of 110 possible states with S_T, the total spin of the Mn_4 cluster, ranging from 0 to 9.

This eigenvalue expression and the corresponding Van Vleck equation were then used to least-squares-fit the experimental data measured in the 5−300 K range (Figure 2). Data below 15 K were omitted in the fitting because zero-field splitting and Zeeman effects likely dominate in this temperature range. With the temperature-independent paramagnetism (TIP) fixed at 600 × 10^{-6} cm^3 mol^{-1}, a good fit was achieved, with final optimized parameters being $g = 1.84$, $J_{wb} = 0.40$ cm^{-1}, and $J_{bb} = 8.1$ cm^{-1}. These values correspond to a ground state with (S_T, S_A, S_B) = (9, 4, 5). The solid line in Figure 2 illustrates this fit, which can be seen to be reasonable. Thus, in this approximate model the desolvated complex **1** is indicated to have a $S_T = 9$ ground state. Unfortunately, several other "fits" (local minima) of the same data could be found, where the ground state of complex **1** has S_T values of 8 and 7, in addition to the $S_T = 9$ value. Considerable effort was made to fit the data to an exact three J value model, where the 900 × 900 spin Hamiltonian matrix was diagonalized in each least-squares fitting cycle. Even with parallel processing on a supercomputer, this proved to be inconclusive, a fact that is likely due to the close energy proximity of two (or more) states at the lowest energy. With the data in Figure 2, we have to conclude that the ground state of complex **1** has a spin of $S_T = 8 \pm 1$.

Similar $\chi_M T$ vs temperature data are also presented in Figure 2 for the hydrated complex **1**·2.5H_2O. Regardless of the details of the fitting of the data for **1** and **1**·2.5H_2O, it is clear from Figure 2 that the data for the hydrated complex exhibit a higher $\chi_M T$ maximum at low temperature. This suggests that **1**·2.5H_2O has a larger spin ground state than does complex **1**. Different preparations of this complex were examined to find that this observation is reproducible. A least-squares fit of the data for **1**·2.5H_2O with the above Kambe model shows that this hydrated complex has a ground-state spin of $S_T = 9$. The solid in Figure 2 illustrates a fit with the parameters $g = 1.89$, $J_{wb} = 1.1$ cm^{-1}, and $J_{bb} = 8.7$ cm^{-1}.

An analysis of variable-field magnetization data (vide infra), taken at the lowest temperatures, can more directly determine the spin of the ground state. That is, if only (a component of) the ground state is populated in the 2.0−4.0 K range in fields of 20−50 kG, then variable-field magnetization data can be used to determine the ground-state spin in the presence of a magnetic field.

Direct Current Magnetization vs Magnetic Fields. To confirm the ground spin state and to determine the magnitude of the zero-field splitting, dc magnetization vs field measurements were made at applied magnetic fields of 20, 30, 40, and 50 kG in the 2.0−4.0 K range for restrained samples of **1** and **1**·2.5H_2O. The data in Figure 4 are shown as reduced magnetization $M/(N\mu_B)$ plotted vs H/T, where M is the magnetization, N is Avogadro's number, μ_B is the Bohr magneton, and H is the magnetic field. For complexes populating only the ground state and with no zero-field splitting the magnetization follows the Brillouin function and the isofield lines all superimpose and saturate at a value of gS. The data in Figure 4 show that the isofield lines do not superimpose for either complex **1** or **1**·2.5H_2O, indicating that the ground state is zero-field-split.

(77) Bolcar, M. A.; Aubin, S. M. J.; Folting, K.; Hendrickson, D. N.; Christou, G. *Chem. Commun*. **1997**, 1485.

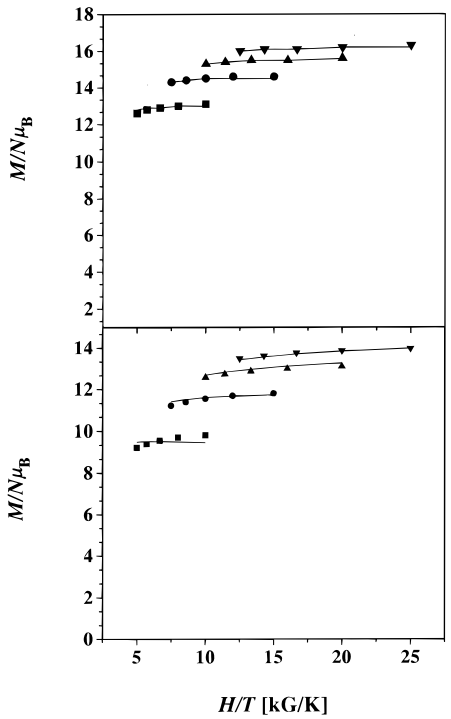

Figure 4. Plot of the reduced magnetization $M/(N\mu_B)$ vs the ratio of the external field and the absolute temperature. The top diagram shows the data for complex **1** measured at 20 (■), 30 (●), 40 (▲), and 50 (▼) kG in the 2−4 K range. The data were fit (see text) assuming only the ground state is populated; the solid lines represent the fits. The bottom diagram illustrates the data and fit for the hydrated complex **1**·2.5H_2O.

It can be seen in Figure 4 that the magnetic field saturation values of complexes **1** and **1**·2.5H_2O are different. For complex **1** in an applied field of 50 kG the reduced magnetization at 2.0 K is 14.0$N\mu_B$, which is appreciably less than the value of 16.3$N\mu_B$ obtained for complex **1**·2.5H_2O at 50 kG and 2.0 K. The $M/(N\mu_B)$ vs H/T data for each of these two complexes were fit using a model that assumes only that the ground state is populated in the 2.0−4.0 K and 20−50 kG ranges. A spin Hamiltonian including an isotropic Zeeman interaction and axial zero-field spitting ($D\hat{S}_z^2$) was used to least-squares-fit the data. The matrix was diagonalized on each cycle, and a powder average was calculated.

The reduced magnetization data for the nonsolvated complex **1** were fit assuming a $S_T = 8$ ground state with the parameters of $g = 1.83$ and $D/k_B = -0.35$ K. These data could not be fit with either $S_T = 9$ or $S_T = 7$, for the resulting g values were unreasonable. Fitting the reduced magnetization data for the hydrate **1**·2.5H_2O was only possible with $S_T = 9$. The fitting parameters were found to be $g = 1.93$ and $D/k_B = -0.37$ K. Thus, the fitting of the variable-field magnetization data clearly indicates that complex **1** has a $S_T = 8$ ground state, whereas complex **1**·2.5H_2O has a $S_T = 9$ ground state.

High-Frequency EPR. Verification of the $S = 9$ ground state for complex **1**·2.5H_2O was obtained by means of high-frequency EPR (HFEPR). This technique is ideally suited for complexes that have appreciable zero-field splitting and/or an integer-spin ground state.[78−80] Since the microwave energies employed (>100 GHz frequency) are relatively large, it is possible to observe direct transitions between the zero-field split components of the large-spin ground state. HFEPR has been used to characterize the ground state of several high-spin complexes.[66,80,81] An analysis of HFEPR spectra can give the sign and precise values for the zero-field splitting parameters. In an ideal case, the spin of the ground state can be determined by simply counting the number of peaks in the fine structure, and the zero-field splitting can be evaluated from the spacing between successive peaks in the fine structure.

The microcrystallites of a SMM orient in a moderate magnetic field so that the principal component (z axis) of the susceptibility tensor for each molecule is parallel to the direction of the external field if all molecules are aligned in the crystal. The HFEPR spectrum for such an oriented microcrystalline sample only shows the parallel EPR signal ($g_{\parallel}$). In this case, the simplest spin Hamiltonian is given by

$$\hat{H} = g\mu_B \hat{H}\cdot\hat{S} + D[\hat{S}_z^2 - (^1/_3)S(S+1)] \qquad (4)$$

In this equation μ_B is the Bohr magneton and g is Lande's factor. The first term is the Zeeman term, and the second is the axial zero-field interaction term. The parameter D gauges the magnitude of the axial zero-field spitting of the ground state. The resonance field at which a transition occurs between the M_s and $M_s + 1$ zero-field components of the ground state is given in

$$H_r = \frac{h\nu}{g\mu_B} - (2M_s + 1)D' \qquad (5)$$

where $h\nu$ is the microwave energy and $D' = D/(g\mu_B)$ for the parallel EPR transitions.

HFEPR spectra were recorded at 218.0, 328.4, and 436.0 GHz in the 4.5−30 K range for an oriented microcrystalline sample of complex **1**·2.5H_2O. Figure 5 shows the 218.0 GHz spectra taken at 4.5 and 30 K. Examination of the 4.5 K spectrum shows that there are basically three regions of transitions: ca. 4, 8, and 12 T. The features seen at ca. 4 T are due to the 218.0 GHz irradiation, whereas those at 8 and 12 T are due to the 328.4 and 436 GHz microwaves, respectively. This was confirmed by independent spectra run at these higher frequencies. In the HFEPR experiment, high-pass filters block out the lower frequency harmonics but not the higher harmonics. Thus, with 220 GHz irradiation, peaks that arise from 330 and 440 GHz are always observed.

It can be seen in Figure 5 that many more peaks are seen in the 30 K spectrum of complex **1**·2.5H_2O than in the 4.5 K spectrum. Fine structure patterns are clearly seen in the 30 K spectrum. At 4.5 K only the lowest energy M_s zero-field component of the ground state is thermally populated. At 30 K several M_s levels are populated and many other transitions are seen. Since the new transitions in each fine structure group occur at higher fields than the most intense peak seen in the 4.5 K spectrum, it can be concluded that the zero-field splitting parameter D is less than 0. If D is greater than 0, then the new transitions seen at the higher temperatures would be expected at lower fields.

Close examination of the fine structure observed in the 30 K spectrum in the ca. 3.5−7.5 T region shows that there is more than one fine structure pattern at 218.0 GHz. In the 4.5 K spectrum, clearly the most intense peak is seen at 3.959 T. Thus, the 3.959 T peak in the 30 K spectrum can be assigned as the leading peak in the dominant fine structure pattern seen. The two lower intensity peaks seen at fields less than 3.959 T must

(78) Brunel, L.-C.; Barra, A.-L.; Martinez, G. *Physica B* **1995**, *204*, 298.
(79) Barra, A.-L.; Brunel. L.-C.; Gatteschi, D.; Pardi, L.; Sessoli, R. *Acc. Chem. Res*. **1998**, *31*, 460.
(80) Barra, A.-L.; Caneschi, A.; Gatteschi, D.; Sessoli, R. *J. Am. Chem. Soc*. **1995**, *117*, 8855.
(81) (a) Barra, A.-L.; Gatteschi, D.; Sessoli, R. *Phys. Rev. B*. **1997**, *56*, 8192. (b) Barra, A.-L.; Caneschi, A.; Gatteschi, D.; Sessoli, R. *J. Magn. Magn. Mater*. **1998**, *177−181*, 709.

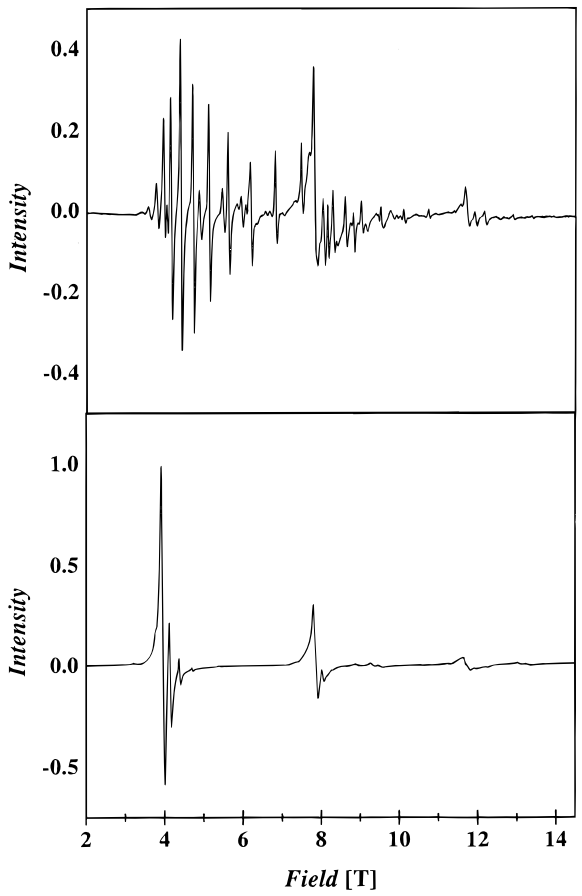

Figure 5. HFEPR spectra recorded at 218 GHz for a microcrystalline sample of complex **1**·2.5H_2O that had been oriented in a strong field. The top plot is of the 30 K spectrum, whereas the 4.5 K spectrum is shown in the bottom plot.

Table 3. Resonant Field Transitions for $[Mn_4(O_2CMe)_2(pdmH)_6](ClO_4)_2$·2.5$H_2O$.

transition	resonance field					
	218.058 GHz		328.419 GHz		436.024 GHz	
$M_s \rightarrow M_s + 1$	exp	calc	exp	calc	exp	calc
−9.0 → −8.0	3.959	3.995	7.896	7.958	11.736	11.823
−8.0 → −7.0	4.145	4.076	8.084	8.039	11.925	11.904
−7.0 → −6.0	4.391	4.296	8.329	8.259	12.173	12.124
−6.0 → −5.0	4.707	4.636	8.648	8.600	12.453	12.465
−5.0 → −4.0	5.113	5.079	9.059	9.042	12.888	12.907
−4.0 → −3.0	5.605	5.604	9.556	9.568	13.369	13.432
−3.0 → −2.0	6.173	6.194	10.114	10.158	13.931	14.023
−2.0 → −1.0	6.805	6.831	10.778	10.794		
−1.0 → 0.0	7.473	7.495	11.432	11.459		
0.0 → 1.0	8.141	8.168				
1.0 → 2.0	8.806	8.883				
2.0 → 3.0	9.514	9.469				
3.0 → 4.0	10.098	10.059				
4.0 → 5.0	10.734	10.585				

be part of other signals. In Table 3 are summarized the peaks we have identified that belong to the main fine structure pattern seen at 218 GHz. A new sample of **1**·2.5H_2O was prepared and HFEPR spectra for this second sample showed that the relative intensities of the different groupings do change from one sample to another. It has to be concluded that in addition to the main fine structure pattern there are one or two other patterns present. There could well be some small amount of the nonsolvated complex **1** or some other modified form of the complex present that gives rise to the weaker signal.

In addition to 218 GHz, 30 K spectra were run for **1**·2.5H_2O at 328.4 and 436 GHz. Table 3 lists the resonances observed

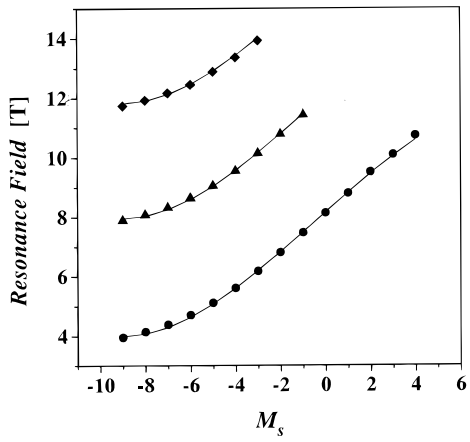

Figure 6. Plot of the resonance field vs the M_s number for the HFEPR transitions between the M_s and (M_s + 1) zero-field components of the ground state of complex **1**·2.5H_2O. HFEPR data were measured at 218.0, 328.4, and 436.0 GHz. The solid lines represent a fit of the data to the spin Hamiltonian given in eq 6.

for all three frequencies. All of the resonance positions listed in Table 3 were analyzed to determine the spin and zero-field splitting parameters of the ground state. All of the data are plotted in Figure 6 as resonance field vs the M_s value for each $M_s \rightarrow (M_s + 1)$ transition. This plot was made assuming the ground state has $S = 9$, and therefore in a field the lowest energy level has $M_s = -9$. Thus, at 218 GHz and 30 K the $M_s = -9$ to $M_s = -8$ transition is seen at 3.959 T. From Figure 6 it is clear that the resonance field positions do *not* exhibit a linear dependency on M_s, as expected from eq 5. These data were best accommodated by assuming $S = 9$ and using the spin Hamiltonian given in

$$\hat{H} = g\mu_B \hat{H}\cdot\hat{S} + D[\hat{S}_z^2 - (^1/_3)S(S+1)] + 35B_4^0\hat{S}_z^4 \quad (6)$$

The quartic longitudinal zero-field interaction term, $35B_4^0\hat{S}_z^4$, is needed to fit the data. This term was also employed to fit HFEPR data for Mn_{12}[81] and Mn_4[63b] SMM's.

The resonance field data for all three frequencies were fit to eq 6 by adopting the eigenfield approach with the downhill simplex method.[82] The solid lines in Figure 6 correspond to this fit of the data assuming a $S = 9$ ground state. The fitting parameters were found to be $g = 1.99(1)$, $D = -0.45(1)$ K, and $B_4^0 = 2.9(3) \times 10^{-5}$ K. When the ground-state spin was taken as $S = 8$, the fitting parameters were found to be $g = 2.10(1)$, $D = -0.47(1)$ K, and $B_4^0 = 4.1(4) \times 10^{-5}$ K. Since $g = 2.10$ is unreasonable for a complex made up of Mn^{III} and Mn^{II} ions[83] and since the variable-field magnetization data indicated $S = 9$, it has to be concluded that complex **1**·2.5H_2O does indeed have a $S = 9$ ground state.

Future HFEPR experiments are planned for the nonsolvated complex **1**; however, this is made difficult by the ease of hydration of this complex.

Alternating Current Magnetic Susceptibility. Complex **1** has a $S = 8$ ground state, whereas complex **1**·2.5H_2O has a $S = 9$ ground state. In both cases there is appreciable magnetic anisotropy due to the zero-field (DS_z^2) interaction. As shown in Figure 7, for a $S = 8$ complex, the combination of a large spin and anisotropy leads to a potential-energy barrier for reversal of the direction of magnetization for a molecule. Zero-

(82) Belford, B. B.; Belford, R. L.; Burkhalter, J. F. *J. Magn. Reson.* **1973**, *11*, 251.
(83) Barra, A.-L.; Gatteschi, D.; Sessoli, R.; Abbati, G. L.; Cornia, A.; Fabretti, A. C.; Uytterhoeven, M. G. *Angew. Chem., Int. Ed.* **1997**, *36*, 2329.

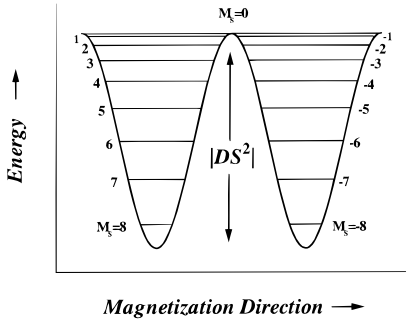

Figure 7. Plot of the potential energy vs magnetization direction for a single-molecule magnet with a $S = 8$ ground state split by axial zero-field splitting. The potential energy barrier height is $U = |D\hat{S}_z^2|$.

field interactions split the $S = 8$ state into the $M_s = \pm 8, \pm 7, ..., \pm 1, 0$ levels depicted in Figure 7. When $D < 0$ in zero applied field, the $M_s = +8$ and $M_s = -8$ states are the lowest in energy. The $M_s = -8$ state can be viewed as the "spin up" state and the $M_s = +8$ state as the "spin down" state. The double-well diagram of Figure 7 shows how the potential energy of one molecule changes as it reverses its direction of magnetization from "spin up" to "spin down". The potential-energy barrier is given by $U = |D\hat{S}_z^2|$.

At low temperatures where the thermal energy is less than the barrier height in Figure 7, slow magnetization relaxation is observed for SMM's. The ac magnetic susceptibility can be used to determine the rate at which a SMM can convert from "spin up" to "spin down". The ac field is oscillated at a set frequency. When this frequency equals the rate of magnetization reversal, a maximum in the out-of-phase ac susceptibility (χ_M'') is observed. At a given frequency of oscillation of the ac field, the temperature of a complex is varied to find a maximum in χ_M''.

The ac susceptibility data were collected for complexes **1** and **1**·2.5H_2O. Initially, for complex **1** it was found using a MPMS2 SQUID that the maxima in χ_M'' vs temperature were found to generally fall at lower temperatures than the 1.7 K lower limit of the instrument. Only at 1000 Hz was the maximum in the χ_M'' vs temperature plot visible.[84] As a result, ac susceptibility measurements were carried out by cooling the sample with a ^{3}He−^{4}He dilution refrigerator. In this manner it was possible to collect data in the 0.4−3.5 K range. Eleven different ac frequencies were used in the range 1.1−995 Hz. Figure 8 shows the data collected in an ac field oscillating at 995, 495, 170, 57, and 10 Hz. At 995 Hz, there is a decrease in the in-phase ac susceptibility χ_M' below 2.5 K such that $\chi'_M T = 19$ cm^3 mol^{-1} K at 2.5 K and drops to $\chi'_M T = 2.7$ cm^3 mol^{-1} K at 1.0 K. In this same temperature region the χ_M'' signal appears and becomes a maximum at 2.03 K, the temperature at which the rate of magnetization reversal for an individual molecule equals the inverse of the frequency of oscillation of the ac field. When 11 different frequencies of ac field oscillation were employed, it was possible to tabulate rates of magnetization reversal at 11 different temperatures, as given in Table 4.

The magnetization relaxation rate data obtained from the ac data for complex **1** were fit to the Arrhenius equation $\tau = \tau_0 e^{-\Delta E/(kT)}$. In this equation for the relaxation time τ, ΔE is the activation energy, k is Boltzmann's constant, and τ_0 is is the preexponential factor. Figure 9 gives a plot of $\ln(1/\tau)$ vs $1/T$, where the solid line represents the least-squares fit of the data to the Arrhenius equation. From the fit the activation energy ΔE was found to be 17.3 K with a preexponential factor of 2.54×10^{-7} s. This value of ΔE is to be compared with the thermodynamic barrier of = 22.4 K, calculated for complex **1** with the values of $S = 8$ and $D = -0.358$ K, as obtained in fitting the variable-field magnetization data. It is quite reasonable that $U > \Delta E$ because the magnetization direction reversal of a SMM may involve not only a thermal activation over the potential energy barrier but also quantum tunneling of the direction of magnetization. In fact, for all single-molecule magnets studied it has been found that $U > \Delta E$. Quantum tunneling of the direction of magnetization has been conclusively established.

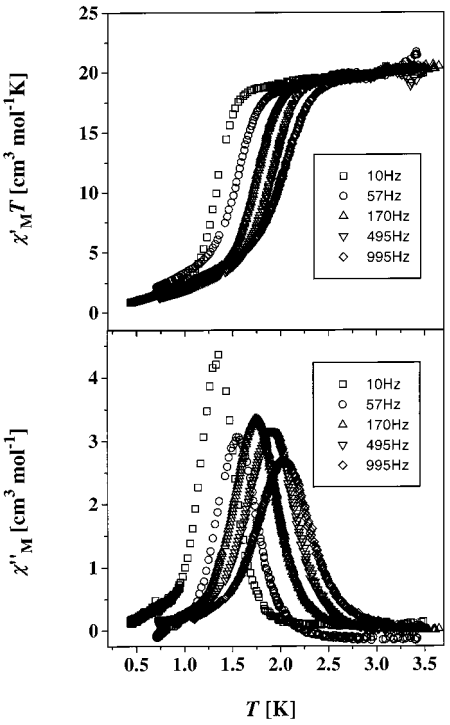

Figure 8. Plots of $\chi'_M T$ (top) and χ_M'' (bottom) vs temperature for a polycrystalline sample of complex **1** in a 1.0 G ac field oscillating at the indicated frequencies, where χ_M' and χ_M'' are the in-phase and the out-of-phase ac magnetic susceptibilities, respectively.

Table 4. Out-of-Phase Alternating Current Magnetic Susceptibility Results for Two Forms of Complex **1**

$[Mn_4(O_2CMe)_2(pdmH)_6](ClO_4)_2$ (**1**)			
ac frequency (Hz)	peak temp [K][a]	$\ln(1/\tau)$[b]	$1/T$ [K]
995	2.03	6.903	0.493
495	1.902	6.205	0.526
170	1.742	5.136	0.574
94	1.653	4.575	0.605
57	1.541	4.043	0.649
31	1.505	3.434	0.664
16	1.394	2.773	0.717
10	1.332	2.303	0.751
5.7	1.312	1.740	0.763
2.7	1.18	0.993	0.847
1.1	1.157	0.095	0.864
$[Mn_4(O_2CMe)_2(pdmH)_6](ClO_4)_2$·2.5$H_2O$ (**1**·2.5H_2O)			
ac frequency (Hz)	peak temp [K][a]	$\ln(1/\tau)$[b]	$1/T$ [K]
1250	2.332	7.131	0.429
1000	2.277	6.908	0.439
750	2.214	6.620	0.452
500	2.13	6.215	0.469
250	1.996	5.521	0.501

[a] This is the temperature where there is a maximum in the out-of-phase ac magnetic susceptibility χ_M''. [b] This is the natural logarithm of the inverse of the magnetization relaxation time calculated from the frequency of the ac magnetic field.

(84) Brechin, E. K.; Yoo, J.; Nakano, M.; Huffman, J. C.; Hendrickson, D. N.; Christou, G. *Chem. Commun.* **1999**, 783.

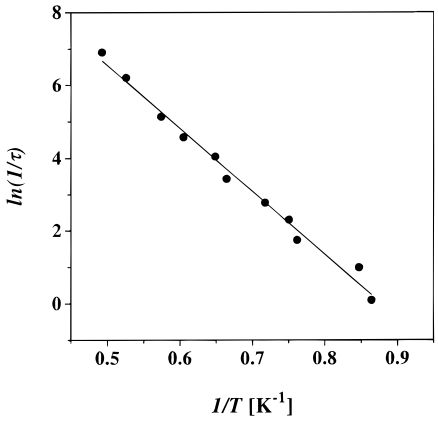

Figure 9. Plot of the natural logarithm of the magnetization relaxation rate [ln(1/τ)] vs the inverse of the absolute temperature. The solid line represents a least-squares fit of the data to the Arrhenius equation (see text).

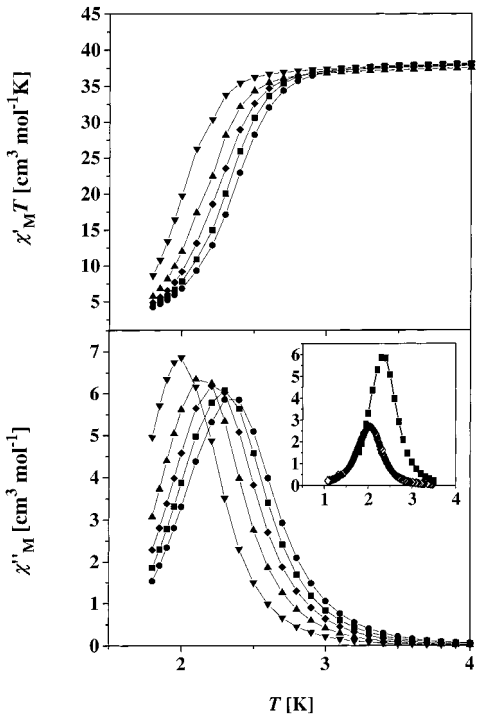

Figure 10. Plots of $\chi'_{M}T$ (top) and χ_{M}'' (bottom) vs temperature for a polycrystalline sample of complex **1**·2H_2O in a 1.0 G ac field oscillating at the following frequencies: (●) 1250, (■) 1000, (♦) 750, (▲) 500, and (▼) 250 Hz. The inset in the bottom diagram gives a comparison of the data for complexes **1** and **1**·2.5H_2O, each measured at 1000 Hz.

The hydrated complex **1**·2.5H_2O was also characterized with ac magnetic susceptibility. The ac susceptibility measurements were performed on the same sample of complex **1**·2.5H_2O as was used in the dc susceptibility experiments. The results are shown in Figure 10. A comparison with the data shown in Figure 8 for complex **1** shows that the χ_{M}'' peaks for the hydrated complex **1**·2.5H_2O occur at higher temperatures than for complex **1**. For example, at a frequency of ca. 1000 Hz there is a shift of the χ_{M}'' peak from 2.0 K for complex **1** to 2.3 K for complex **1**·2.5H_2O. The data for the hydrated complex were also least-squares-fit to the Arrhenius equation to give an activation energy of $\Delta E = 16.7$ K. This is to be compared with $U = 30$ K evaluated for this hydrated complex from the dc magnetization data. There is a small change from $\Delta E = 17.3$ K for the $S = 8$ complex **1** to $\Delta E = 16.7$ K for the $S = 9$ complex **1**·2.5H_2O.

Concluding Comments

The synthesis, X-ray structure, and magnetic properties of a new type of single-molecule magnet, $[Mn_4(OAc)_2(pdmH)_6](ClO_4)_2$ (**1**), were presented. The X-ray structure shows a valence-trapped, mixed-valent $Mn^{III}_2Mn^{II}_2$ complex. Since it has been shown previously that the electronic structures of mixed-valence complexes in the solid state are quite sensitive to the nature of solvate molecules present in the crystals,[85] it was reasonable to find that different solvates of **1** show different properties. The nonsolvated complex **1** was shown with magnetization data to have a $S = 8$ ground state, whereas the hydrated complex **1**·2.5H_2O has a $S = 9$ ground state. This difference is reflected in the ac magnetic susceptibility responses of the two forms of the complex. Clearly, complexes **1** and **1**·2.5H_2O are single-molecule magnets, and at temperatures below ca. 2 K, there is slow magnetization relaxation.

It will prove interesting to compare the magnetization relaxation characteristics of complex **1** with those of $[Mn_4O_3Cl(O_2CCH_3)_3(dbm)_3]$ (**3**). Complex **3** has a $Mn^{IV}Mn^{III}_3$ distorted cubane construction and has been shown to have a $S = {}^9/_2$ ground state with $D = -0.53$ cm^{-1}. Steps were observed on the magnetization hysteresis loop, showing that complex **3** is a single-molecule magnet. Complex **3** shows a temperature-dependent magnetization relaxation in the 0.6−2.2 K range with an activation energy of $\Delta E = 11.8$ K. It was most interesting to find that in the range 0.39−0.60 K the magnetization relaxation rate is temperature-independent. This $S = {}^9/_2$ single-molecule magnet exhibits a tunneling of its direction of magnetization at a rate of 3.2×10^{-2} s^{-1} in the 0.39−0.60 K range. Resonant magnetization tunneling is occurring between the lowest energy levels, $M_s = -{}^9/_2$ and $M_s = +{}^9/_2$, of the ground state.

Complex **1** has a larger ground-state spin ($S = 8$) and smaller axial zero-field splitting ($D = -0.25$ cm^{-1}) than complex **3**. Preliminary experiments show that complex **1** also exhibits quantum tunneling of the direction of magnetization[86] that occurs with a temperature-independent rate that is considerably slower than the 3.2×10^{-2} s^{-1} rate shown by complex **3**.[63b] However, the temperature-independent tunneling rate of complex **1** does not appear to be as slow as the $\sim 10^{-8}$ s^{-1} rate reported for the $S = 10$ complex $[Mn_{12}O_{12}(O_2CCH_3)_{16}(H_2O)_4]$·4$H_2O$·2$HO_2CCH_3$.[88] The origin of the resonant magnetization tunneling in these single-molecule magnets is an actively pursued research topic.[18−21,37,87] Transverse components of either zero-field interactions or magnetic fields determine the rate of resonant magnetization tunneling. The transverse magnetic field may be external or it may be from an internal field in the crystal due to neighboring paramagnetic molecules and/or nuclear spins at the Mn ($I = {}^5/_2$) atoms.

Acknowledgment. G.C. and D.N.H. thank the National Science Foundation for support of this research.

Supporting Information Available: X-ray crystallographic files, in CIF format. This material is available free of charge via the Internet at http://pubs.acs.org.

IC000237W

(85) Hendrickson, D. N. In *Mixed-Valency Systems: Applications in Chemistry, Physics, and Biology*; Prassides, K., Ed.; Kluwer Academic Publishers: Dordrecht, 1991; pp 67−90.
(86) Yamaguchi, A.; Ishimoto, H.; Awaga, K.; Yoo, J. S.; Nakano, M.; Hendrickson, D. N.; Brechin, E. K.; Christou, G. *Physica B*, in press.
(87) Friedman, J. R. *Phys. Rev. B* **1998**, *57*, 10291 and references therein.
(88) Paulsen, C.; Pouk, J.-G.; Benbara, B.; Sessoli, R.; Caneschi, A. *J. Magn. Magn. Mater*. **1995**, *140−141*, 1891.